IN-73-CR
NAG5-1713
86922

A SEARCH FOR THE DIPOLE ANISOTROPY OF THE COSMIC X-RAY BACKGROUND

P.24

Tom Evans, Haverford College, Haverford, PA

Advisor, Steve Boughn, Haverford College

Senior Thesis, May 1, 1992

ABSTRACT

We have analyzed x-ray data obtained by the HEAO-1 A2 satellite in order to look for large scale structure in the Cosmic X-Ray Background. The dipole moment of the x-ray background is $\frac{\delta I}{I} = (1.87 \pm .34) \times 10^{-2}$ in a direction, declination= $3.6 \pm 9.4^{\circ}$ and right ascension= $15.9 \pm .2$ hr. This implies a velocity of the Earth with respect to the background of 409.2 ± 74.4 km s^{-1} in the same direction. Comparatively, measurements of the dipole anisotropy of the Cosmic Microwave Background imply a velocity of 369.2 ± 4 km s^{-1} in a direction, declination=$6 \pm 1^{\circ}$ and right ascension=$11.2 \pm .1$ hr [1]. Quoted errors are statistical only. The disparity between the velocities of the x-ray dipole and microwave dipole may be due to residual structure in the x-ray sky or as yet undiscovered systematic errors.

(NASA-CR-190289) A SEARCH FOR THE DIPOLE ANISOTROPY OF THE COSMIC X RAY BACKGROUND Thesis (Haverford Coll.) 24 p CSCL 03B

N92-25504

Unclas
G3/93 0086922

I. INTRODUCTION

In 1977, the HEAO-1 A2 satellite carried out an one year broad band survey of the x-ray sky from energies 0.1 keV to over .5 MeV [2]. The physical origin of the Cosmic X-ray Background (CXB) is still a much debated topic. Diffuse thermal emission from a hot intergalactic gas, bright AGN at high redshift, a new population of bright extragalactic objects, or a combination of these may contribute to the spectrum of the CXB. Regardless of its generation, the CXB does not have a local origin. The observed relative uniformity of the CXB over large angular scales, like the Cosmic Microwave Background, provides a distant reference frame from which large scale motions may be inferred [3].

The peculiar motion of the Earth with respect to this reference frame results in a dipole anisotropy of the X-ray background by virtue of the Doppler effect. The velocity of this motion may be inferred from the magnitude and direction of the dipole. The $3^{o}K$ microwave background (the remnant radiation from the epoch of recombination) provides a complimentary distant reference frame. The origin of the microwave background, as opposed to the CXB, is well understood, thus it provides an important comparison with the velocity measured from the CXB dipole. Because the spectral

index of the CXB is substantially less than that observed in the microwave background, the amplitude of the dipole anisotropy in the CXB is several times that of the microwave dipole anisotropy. Since the signal-to-noise is much lower in the X-ray map than in a typical microwave map, this factor is important in accessing the feasibility of measuring the dipole anisotropy of the CXB.

The goal of this study is to measure the velocity and direction of the peculiar motion of the Earth from the CXB dipole. Of particular interest will be a comparison of the dipole anisotropies of the CXB and the microwave background.

II. BACKGROUND

II.1 THEORETICAL BACKGROUND

The spectrum of the CXB is discussed in detail by Marshall et al., Boldt, and Holt [2,4,5,6]. Data from the HEAO1-A2 satellite, in the 3-50keV energy band, is used to measure the spectrum of the residual CXB. Figure 1 shows the fits by Marshall et al. of the CXB spectrum to a power law, such that,

$$\frac{dN}{dE} \propto E^{-\Gamma}, \qquad (1)$$

where N is the number of photons, and E is the energy [5,6]. At Γ=1.4 the fit is good at E $\leq$ 15keV, however, at higher energies the fit becomes progressively worse. For Γ=1.7, the overall fit to the data is better, but, the fit fails to match the data in the range from 3-50keV [5]. The best fit to the residual CXB corresponds to diffuse free-free emission from a hot, intergalactic gas. Figure 2 shows the best fit to optically thin thermal bremstrahlung by Boldt [4]. The measured background radiation is represented by the expression,

$$\frac{dI}{dE} = 7.8E^{-\alpha} \exp\left(\frac{-E}{kT}\right), \qquad (2)$$

where I is the intensity of the photons, E is the energy, and α is the spectral index, where $\alpha=\Gamma-1$ [2]. The best fit to the CXB corresponds to α=.29 and kT=40keV [2].

Despite the good fit to optically thin thermal bremstrahlung shown in Figure 2, recent Cosmic Background Explorer (COBE) satellite spectral observations have set an upper limit on the size of the intergalactic medium which is a factor of 10 less than that required for the generation of the CXB [6]. Seyfert galaxies, clusters of galaxies, quasars, and bright active galactic nuclei (AGN) are dominant discrete x-ray sources which may contribute to the CXB [2,5,6]. Table 1 shows power-law fits to several classes of

bright AGN [6]. Examination of the spectra exhibited by these sources reveals that they have steeper slopes than that found in the CXB. Marshall et al. show that subtracting the Seyfert contribution from the spectrum of the CXB does not substantially change its shape since the contribution from Seyfert galaxies is small, roughly 12-18% between 4-50keV [5]. Subtraction of galaxy clusters flattens out the CXB spectrum at energies <10keV [5]. There is no simple method of combining the contributions of discrete extragalactic sources to fit the spectrum displayed by the CXB.

Whether the CXB is due to diffuse thermal emission, bright AGN at high redshift, an undiscovered population of distant bright sources, or some combination of these processes, the CXB exhibits uniformity over large angular scales [2,3]. Thus, the CXB is complimentary to the microwave background as defining a distant reference frame from which large scale galactic motions may be measured.

As shown by Raine, the peculiar motion of the Earth with respect to the CXB results in a dipole anisotropy because of the following reasons [7]. Firstly, a moving telescope will collect more photons because it moves with respect to the background. In time dt, the number of photons is increased by a factor of $1+\beta\cos\theta$, where $\beta=\frac{v}{c}$. The intensity of a moving observer, I_υ', in direction θ, is related to the rest frame intensity, I_υ, by

$$I_\upsilon' = (1 + \beta\cos\theta)^3 \, I_\upsilon. \qquad (3)$$

Likewise, the frequency in the rest frame and moving frame is related by,

$$\upsilon' = (1 + \beta\cos\theta)\upsilon. \qquad (4)$$

The observed power-law spectrum of the CXB is, $I_\upsilon = i \, \upsilon^{-\alpha}$.

Compensating for the effects of motion on the observed intensity of the CXB, the expression for I_υ' becomes,

$$I_\upsilon' = (1 + \beta\cos\theta)^{3+\alpha} \, i \, (\upsilon')^{-\alpha}, \qquad (5)$$

where α is the spectral index and i is a constant. Since β is very small, the expression for the dipole amplitude, $\frac{\delta I}{I}$, becomes

$$\frac{\delta I}{I} = (3 + \alpha) \left(\frac{v}{c}\right) \cos\theta \, . \qquad (6)$$

The microwave dipole has a black-body spectrum, which, on the Raleigh-Jeans side, has a spectral index of α=-2. The intensity of the microwave dipole has the form,

$$\frac{\delta T}{T} = \frac{v}{c} \cos\theta, \qquad (7)$$

where T is the temperature of the background which is 2.7°K. For a spectral index of .4, the x-ray dipole amplitude is approximately 3.4 times that of the microwave dipole amplitude.

II.2 EXPERIMENTAL BACKGROUND

The x-ray data for this analysis is accumulated from the A-2 Cosmic X-Ray Experiment on the HEAO1 satellite. The exact details of the experimental system are described by Boldt [2]. The telescope scanned the sky in great circles on the celestial sphere every half-hour. The spin axis of the satellite was pointed towards the sun, moving one degree per day along the ecliptic equator, thus completing a sweep of the entire sky in 180 days. The scan path of the telescope is along lines of ecliptic longitude as shown in Figure 3 [2]. Cosmic x-rays were observed in a broad band from .1keV to .5MeV [2]. X-rays with energies from 2 to 60 keV are considered here.

X-rays were detected in multianode gas proportional counters optimized for low, medium, and high energy x-rays. Propane gas was used for low energy x-rays (.1 - 3keV), Argon gas was used for medium energy x-rays (1.5 - 20keV), and

Xenon gas was used for high energy x-rays (2 - 60keV). The experiment consisted of six detectors, 2 low energy detectors (LED), 1 medium energy detector (MED), and 3 high energy detectors (HED). In order to subtract the offset from the diffuse background, two fields of view (FOV) were associated with each detector since diffuse flux increases linearly with solid angle. One FOV is always 3° x 3° (LFOV), while the other is 3° x 1.5° (SFOV) or 3° x 6° [2]. For diffuse sources, the LFOV has twice the signal as the SFOV. The noise in the data is dominated by photon counting noise. Figure 4 is a cosine-projection map of the x-ray sky for the 3° x 1.5° FOV in galactic coordinates.

III. ANALYSIS

III.1 CLEANING PROCEDURES AND BACKGROUND STRUCTURE

As seen in Figure 4, the x-ray sky contains many bright sources. These sources have to be removed from the map in order to investigate the underlying large-scale structure. First, the map is divided into 24576 square pixels which are 1.296° on a side. The noise associated with each pixel is photon counting noise, which is the square root of the number of photons in each pixel, thus, $\sigma \sim \sqrt{n}$. Extended sources are more easily identified by smoothing the map on a 3° scale.

Bright sources 4σ above the local background are then removed from the map by cutting "rings" of the eight nearest neighbor pixels. Approximately 7000 pixels are cleaned from the data using nearest neighbor cuts at 4σ. Figure 5 shows the cleaned LFOV map with bright sources and a strip ± 20° b^{II} of the Galaxy removed.

To test for systematic time drifts of the instrument, the detector intensity is plotted versus time. Figure 6a and b are plots of the cleaned data for the LFOV and SFOV versus time. Recall that the telescope scans over the whole range of ecliptic latitudes while maintaining a constant ecliptic longitude for each day. Each point on the graph corresponds to a region of the sky 5° in longitude and all latitudes and, therefore, is equivalent to a 5-day block of data. The most striking feature in the time-domain plots is the amount of structure above the noise. To remove a linear time-drift, a two-parameter fit of the form, $At_i + B$, is subtracted from the data. The fits are shown in Figures 6a and b. The LFOV should have two times the amplitude of diffuse background as the SFOV, however, a linear fit to the two maps does not yield the expected 2-1 ratio. This implies that the linear time drift is neither associated with real structure in the sky, nor with a drift in gain of the counter.

To test whether the residual structure in these plots is a systematic drift or real structure, the sky is divided into

three latitude bins of 60°. Figure 7 shows three drift-corrected data-time plots of the cleaned SFOV map. If the residual structure is due to detector offset drift, then one expects the 3 plots to be highly correlated since they represent the same time interval. However, the correlation coefficient between bins (a) and (b) is r=.41; between bins (b) and (c), r=.36; and between bins (a) and (c), r=.07. This indicates that the residuals are not due to time drift, but, rather to some other systematic, or, perhaps to large-scale structure in the sky.

III.2 THE DIPOLE ANISOTROPY

To reduce contributions from unresolved point sources the map is median filtered before fitting the dipole. This consists of dividing the map into 384, 8 x 8 pixel bins and substituting the median intensity for each bin. The noise associated with each median filtered bin is difficult to compute analytically, so a set of fake data is generated in a Monte Carlo calculation to approximate the errors for each bin. The center of each bin is calculated in equatorial coordinates.

The expected dipole structure can be represented by a linear combination of the l=1 spherical harmonics such that,

$$I(\theta,\phi) = I_o + \delta I \sum_{m=-1}^{1} Y_{1m}, \text{ where} \qquad (8)$$

$$Y_{10} = \sqrt{\frac{3}{4\pi}} \cos\theta$$

$$Y_{11} = \sqrt{\frac{3}{8\pi}} \sin\theta \; e^{i\phi}$$

$$Y_{1-1} = \sqrt{\frac{3}{8\pi}} \sin\theta \; e^{-i\phi}.$$

The observation angles are equatorial coordinates, declination = $\frac{\pi}{2} - \theta$, and right ascension = ϕ. The three normalized functions used in the fit are,

$$f_1(\theta_i,\phi_i) = Y_{10} = \sqrt{\frac{3}{4\pi}} \cos\theta_i \qquad (9)$$

$$f_2(\theta_i,\phi_i) = \frac{1}{2}(Y_{11}+Y_{1-1}) = \sqrt{\frac{3}{8\pi}} \sin\theta_i \cos\phi_i$$

$$f_3(\theta_i,\phi_i) = \frac{1}{2i}(Y_{11}-Y_{1-1}) = \sqrt{\frac{3}{8\pi}} \sin\theta_i \sin\phi_i.$$

A least squares fit of a dipole to the data requires the minimization of χ^2,

$$\chi^2 = \sum_{i}^{\#\ \text{of bins}} \frac{(I_i - Af_1(i) - Bf_2(i) - Cf_3(i) - D)^2}{\sigma_i^2}, \quad (10)$$

where σ_i^2 represents the errors for each bin and D is the fit offset, I_o. Minimizing χ^2 with respect to A,B,C, and D leaves 4 linear equations and 4 unknowns. The dipole amplitude, δI, has the form, in terms of A,B, and C,

$$\delta I = \sqrt{\tfrac{3}{4\pi} A^2 + \tfrac{3}{8\pi} B^2 + \tfrac{3}{8\pi} C^2}. \quad (11)$$

IV. DISCUSSION

The dipole amplitude, δI, for the x-ray map in the 2 to 50keV energy range is $(1.87 \pm .34) \times 10^{-2}$. Using equation (6), with I=4.03, the peculiar velocity of the Earth is 409.2 $\pm$ 74.4 km s^{-1}. The dipole has a direction of declination=3.6 $\pm$ 9.4° and right ascension=15.9 $\pm$ .2 hr. The velocity inferred from the microwave dipole is 369.2 $\pm$ 4 km s^{-1} in a direction declination=6 $\pm$ 1° and right ascension=11.2 $\pm$ .1 hr [1]. Quoted errors are statistical only. The ratio, $\frac{v}{c} = 1.2 \times 10^{-3}$ is determined from the dipole in the microwave background; therefore, from equation (6), an amplitude of

approximately 4.2×10^{-3} is expected for the CXB [1]. On the other hand, the bumps in the time-domain--see Figures 6 and 7--are on the order of 10^{-2}, thus, the structure in the time domain is of the same order as the large-scale structure of the dipole. This structure may be the cause of the disparity between the velocities of the x-ray and microwave dipoles.

The relative correlation over large angular scales shown in Figure 7 may suggest the existence of some large scale structure. However, cutting larger numbers of pixels from the data does not substantially reduce the structure shown in the time-domain. This implies that the observed bumps are not due to bright sources in the x-ray sky.

Jahoda and Mushotzky propose that some large scale structure may be due to diffuse x-ray emission from the Galaxy at b^{II} greater than 10° [8]. However, cutting larger regions of the Galaxy, $\pm 30^{\circ}$ b^{II} of the galactic plane, from the map does not give more accurate results of the dipole amplitude. At low energies, $E < 1keV$, the Galaxy exhibits large scale structure well outside the galactic plane [9]. The high energy counterpart to this may be responsible for the observed residual structure in Figures 6 and 7, therefore, an accurate fit to the dipole is difficult. Instead, the expected dipole can be subtracted from the data, leaving the leftover residuals to be investigated for other large scale structure.

Another strong feature in the x-ray sky is the 20° bright region at b^{II}= 18° and l^{II}= 309°, known as the Great Attractor (GA) [9]. However, because of the direction of the GA, as compared to the direction of the CXB dipole, this region cannot account for all of the discrepancies in the dipole amplitude. Also, any structure associated with this region may have galactic origins and, therefore, is an upper limit for large scale galactic effects [9]. Further analysis of the GA region may resolve some of the questions pertaining to the structure observed in the background.

Systematic effects such as the earth's magnetic field,solar effects, or internal systematics may be the cause of some of the structure in the time-domain.

V. ACKNOWLEDGEMENTS

I wish to thank Steve Boughn for his guidance and advice on this project. Also, I would like to thank Keith Jahoda for his input and contributions to the analysis. I also thank Jon Marr for his insightful discussions and aid with this study.

VI. REFERENCES

[1] Boughn, S.B. 1992, preprint.

[2] Boldt, E. 1987, *Physics Rept.*, **146**, 215.

[3] Mushotzky, R. 1989, in press.

[4] Boldt, E. *International Workshop on the X-Ray Background.*, 1.

[5] Marshall, F. et al. 1980, *APJ.*, **235**, 4.

[6] Holt, S. *International Workshop on the X-Ray Background.*, 24.

[7] Raine, D.J. *The Isotropic Universe,* (Adam Hilger LTD., Bristol: 1981) 80.

[8] Jahoda, K. and Mushotzky, R. *International Workshop on X-Ray Background.*, 58.

[9] Jahoda, K. and Mushotzky, R. 1989, *APJ.*, **346**, 638.

VII. FIGURES

Figure 1. CXB data from HEAO1 A-2 for Γ=1.4 and 1.7. The ratio of observed counts for the CXB to that predicted for power-law incident spectra. Statistical errors are shown when larger than the sizes of the symbols [5].

Figure 2. G (the observed CXB spectrum multiplied by $\exp\left(\frac{E}{kT}\right)$), with kT=40keV, as a function of photon energy (E). The circled points shown represent the best-fit thermal model for measurements made with gas proportional counters of the HEAO1 A-2 experiment (Marshall et al. 1980). The power-law straight line indicated corresponds to equation (2) [4].

Table 1. Bright AGN and their associated spectral indices [6].

Figure 3. The HEAO1 A-2 satellite. The collimation angle is always 3 degrees with θ=1.5 degrees. At any instant the FOV is either 3 x 3 or 3 x 1.5 degrees. The instrument scans in great circles along the celestial sphere with the spin axis pointed towards the sun. Ecliptic coordinates are: λ (ecliptic longitude) and β (ecliptic latitude) [2].

Figure 4. Cosine-projection of the x-ray sky in galactic coordinates for the 3° x 3° FOV. The Galaxy is the bright strip across the center of the map between $\pm$~20 degrees.

Figure 5. Cleaned LFOV map. White marks are cleaned pixels.

Figure 6. a) Plot of Intensity versus time for the cleaned SFOV map. b) Plot of intensity versus time for the cleaned LFOV map. The units of intensity are proportional to photon counts. Time is in days, with the first day of observation being 322. The data is binned into five-day periods to reduce the errors.

Figure 7. a) Data versus time from $\beta=-90^\circ$ - -30°. b) Data versus time from $\beta=-30^\circ$ - 30°. c) Data versus time from $\beta=30^\circ$ - 90°. The mean and time-drift is subtracted from the data. The plots are taken from the 3 x 1.5 degree map.

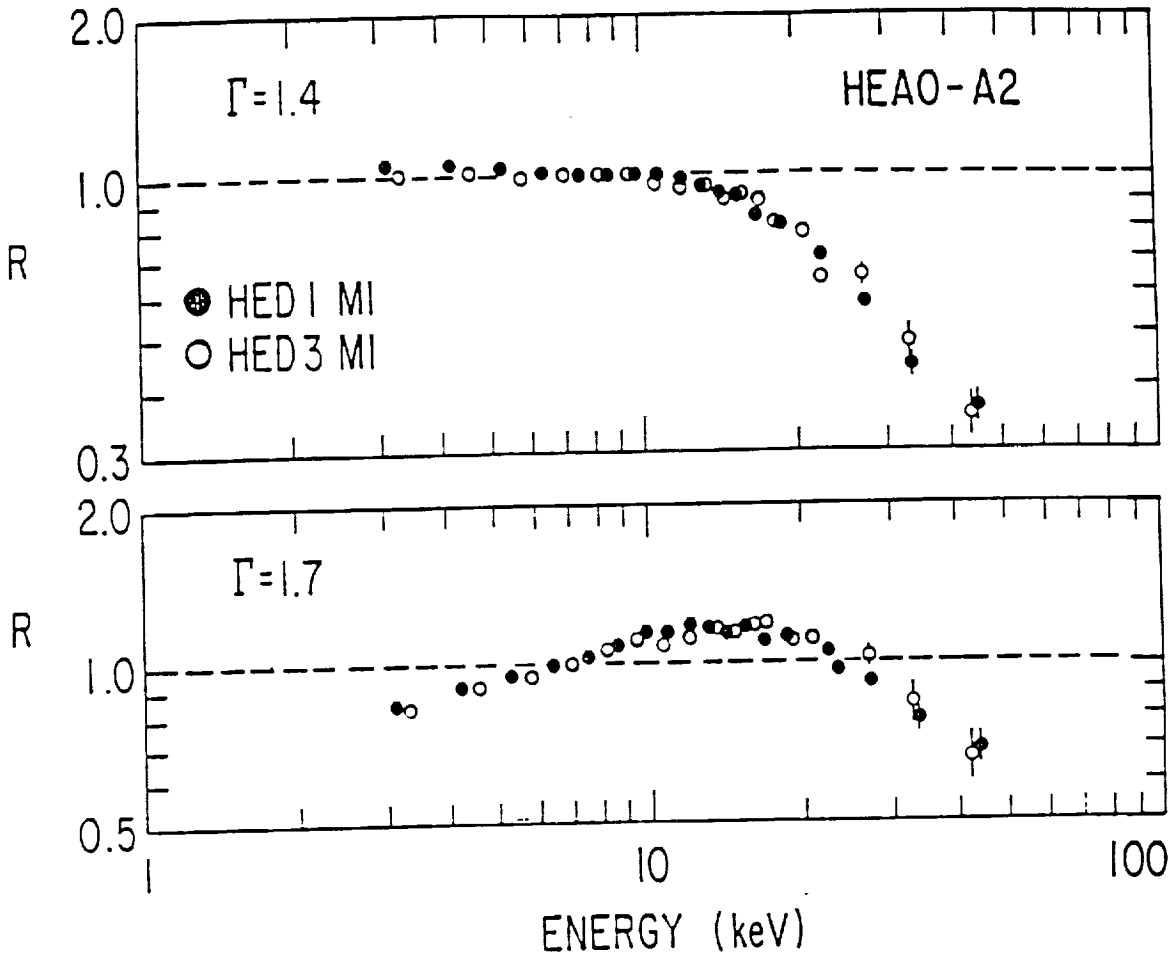

Figure 1. CXB data from HEAO1 A-2 for Γ=1.4 and 1.7. The ratio of observed counts for the CXB to that predicted for power-law incident spectra. Statistical errors are shown when larger than the sizes of the symbols [5].

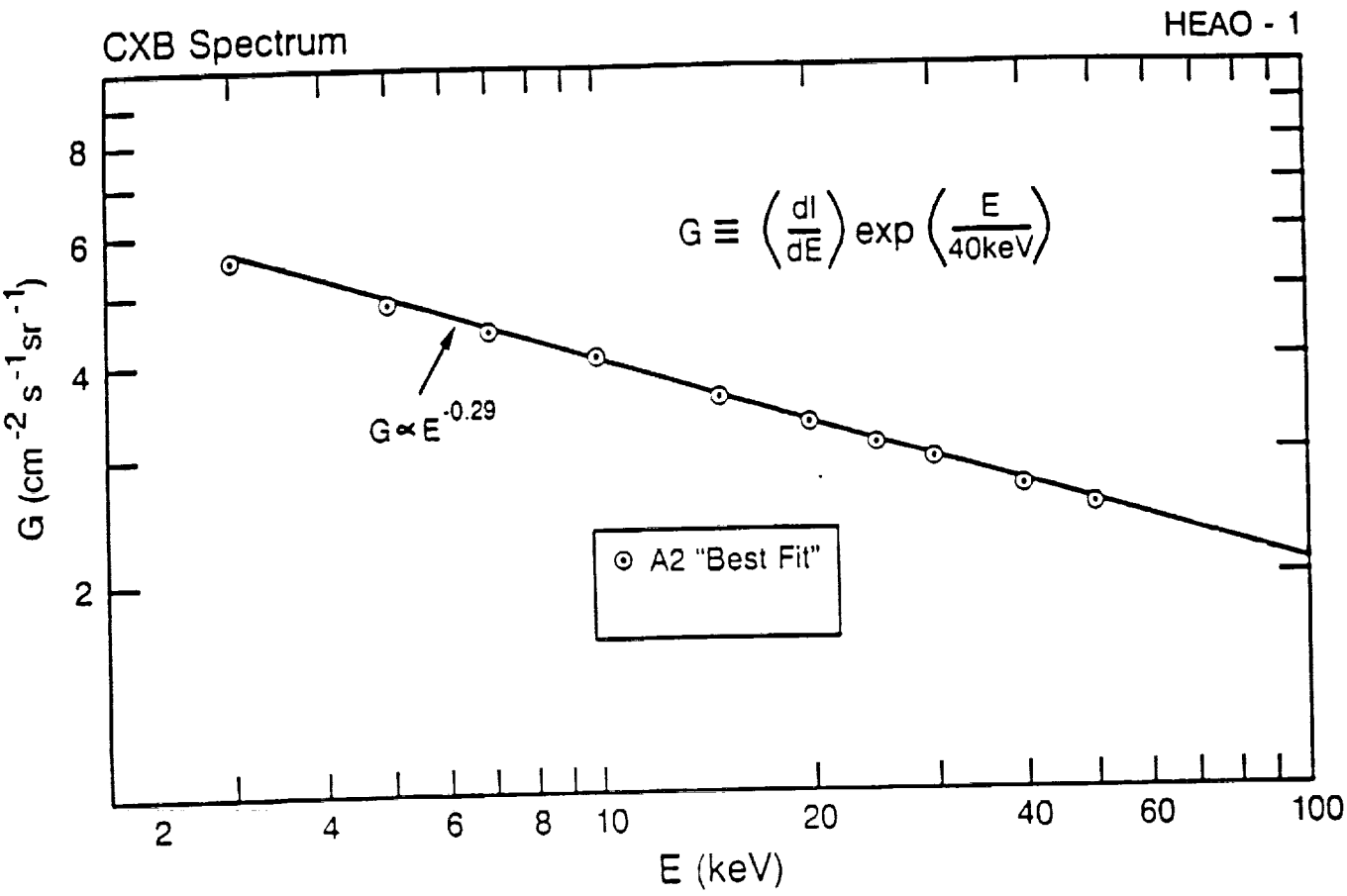

Figure 2. G (the observed CXB spectrum multiplied by $\exp\left(\frac{E}{kT}\right)$, with kT=40keV, as a function of photon energy (E). The circled points shown represent the best-fit thermal model for measurements made with gas proportional counters of the HEAO1 A-2 experiment (Marshall et al. 1980). The power-law straight line indicated corresponds to equation (2) [4].

TYPE	α	KT
Seyfert I	.7	>100keV
Quasars	1.2	>20keV
Clusters of Galaxies	.4	6keV
Pulsar Driven SN	1.1	>100keV
Neutron Star Binaries	1	20keV
CXB	.29	40keV

Table 1. Bright AGN and their associated spectral indices [6].

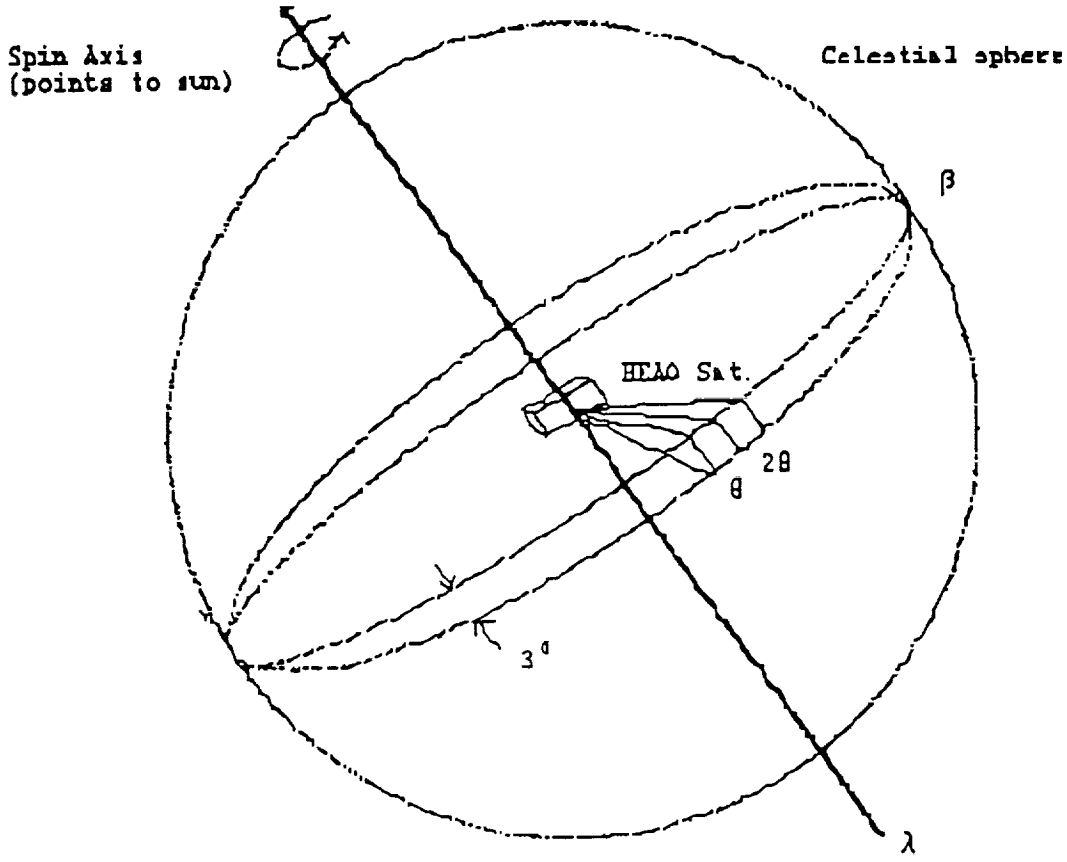

Figure 3. The HEAO1 A-2 satellite. The collimation angle is always 3 degrees with θ=1.5 degrees. At any instant the FOV is either 3 x 3 or 3 x 1.5 degrees. The instrument scans in great circles along the celestial sphere with the spin axis pointed towards the sun. Ecliptic coordinates are: λ (ecliptic longitude) and β (ecliptic latitude) [2].

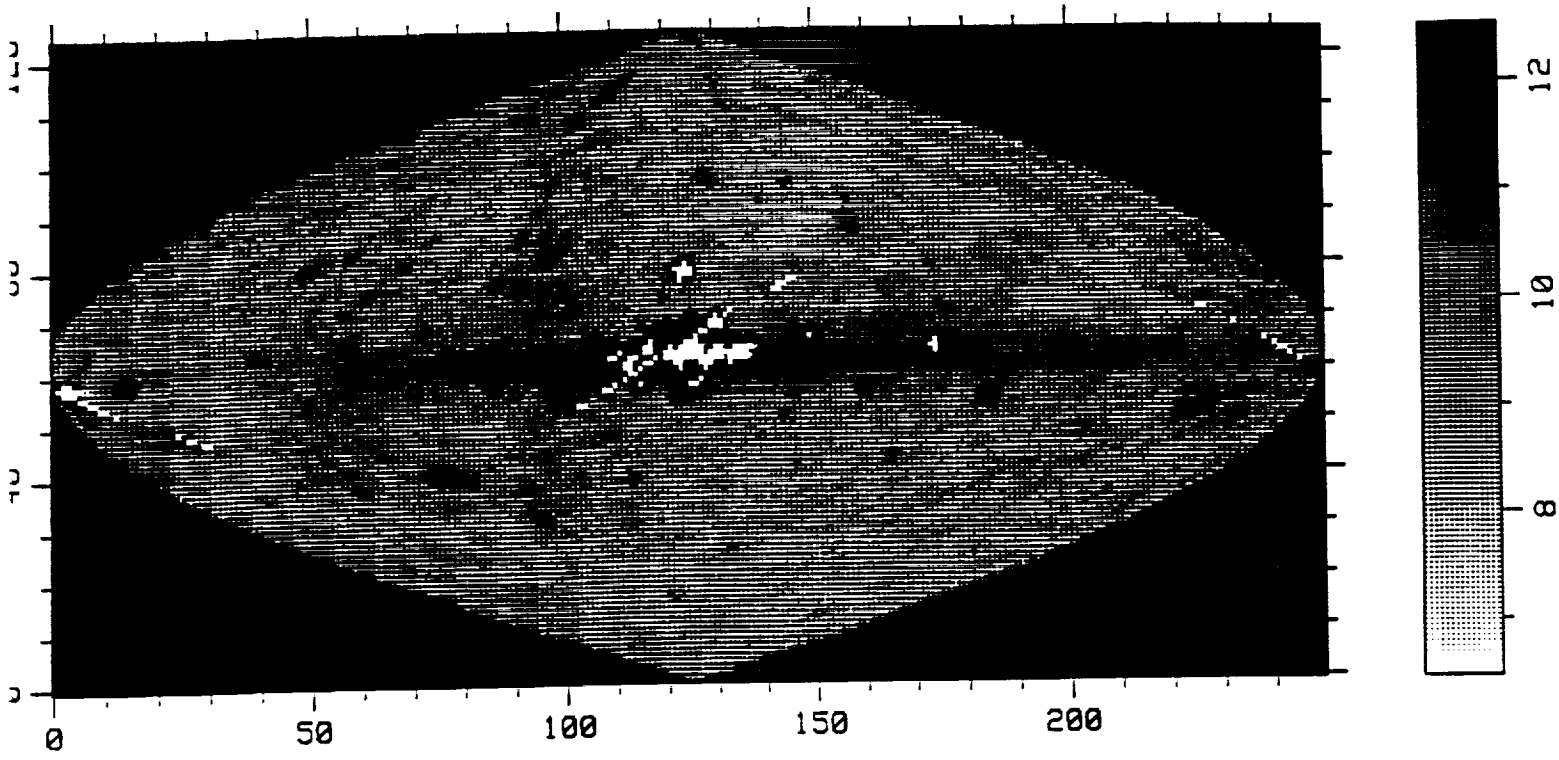

Figure 4. Cosine-projection of the x-ray sky in galactic coordinates for the 3° x 3° FOV. The Galaxy is the bright strip across the center of the map between ±~20 degrees.

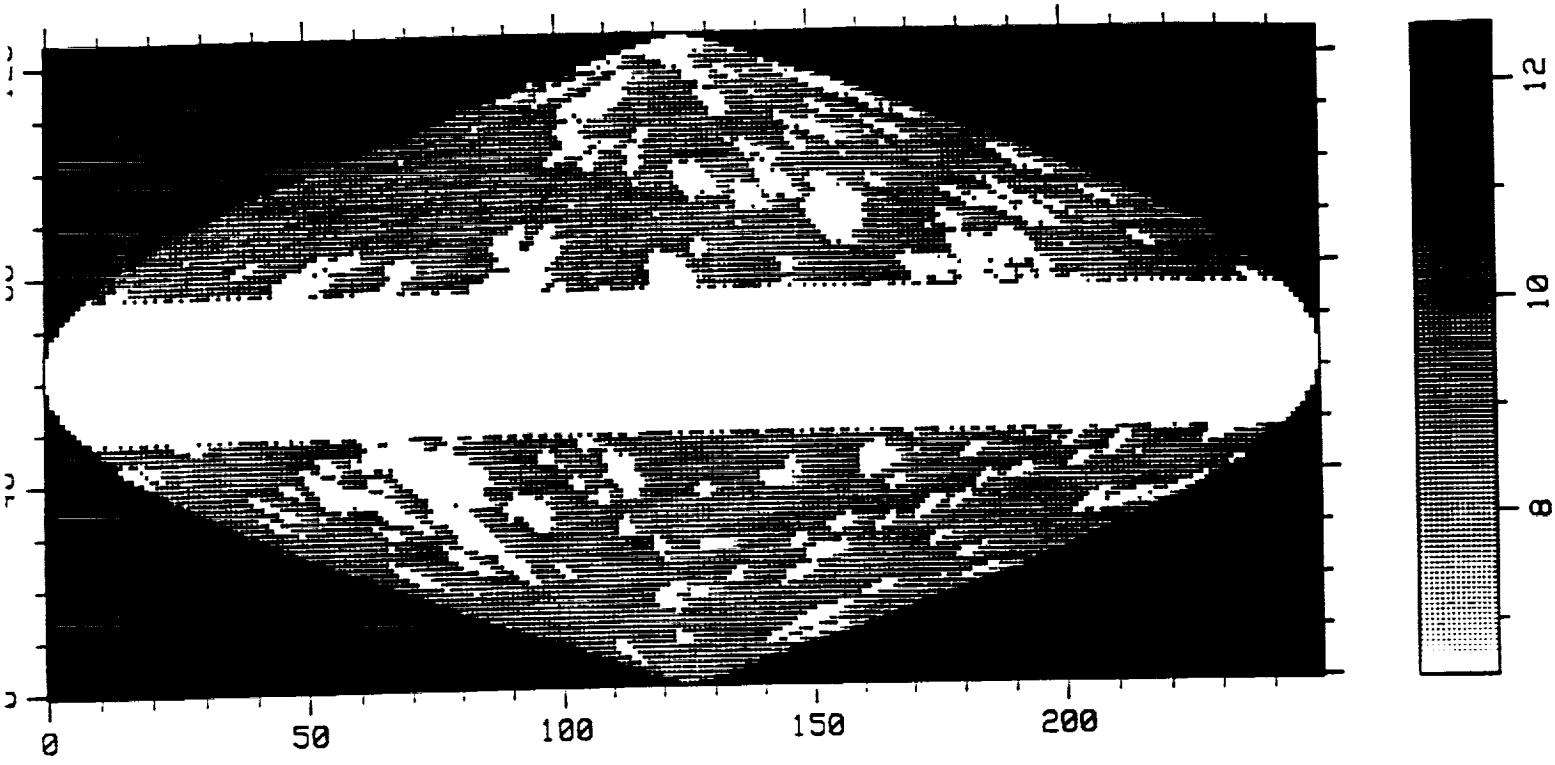

Figure 5. Cleaned LFOV map. White marks are cleaned pixels.

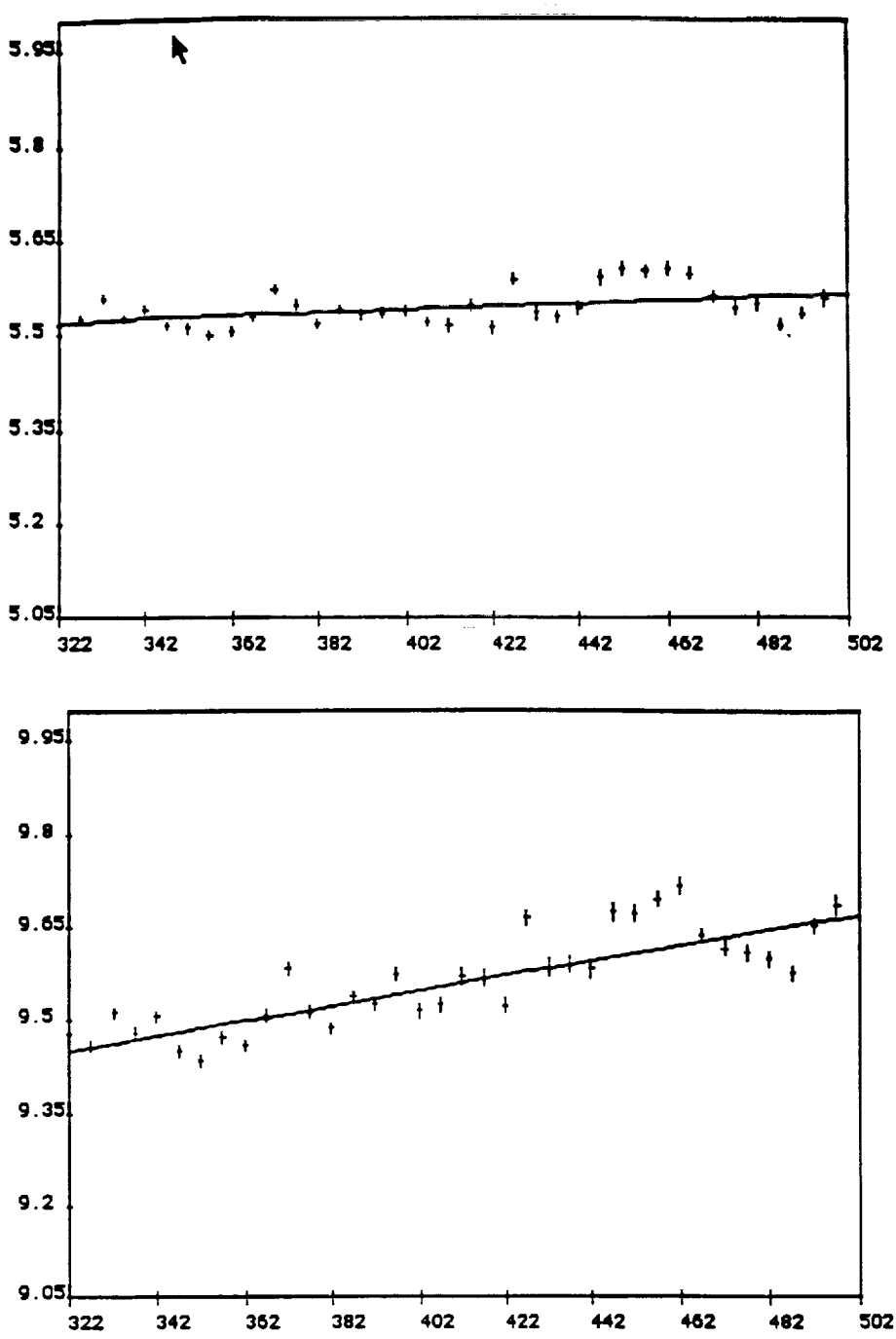

Figure 6. a) Plot of Intensity versus time for the cleaned SFOV map. b) Plot of intensity versus time for the cleaned LFOV map. The units of intensity are proportional to photon counts. Time is in days, with the first day of observation being 322. The data is binned into five-day periods to reduce the errors.

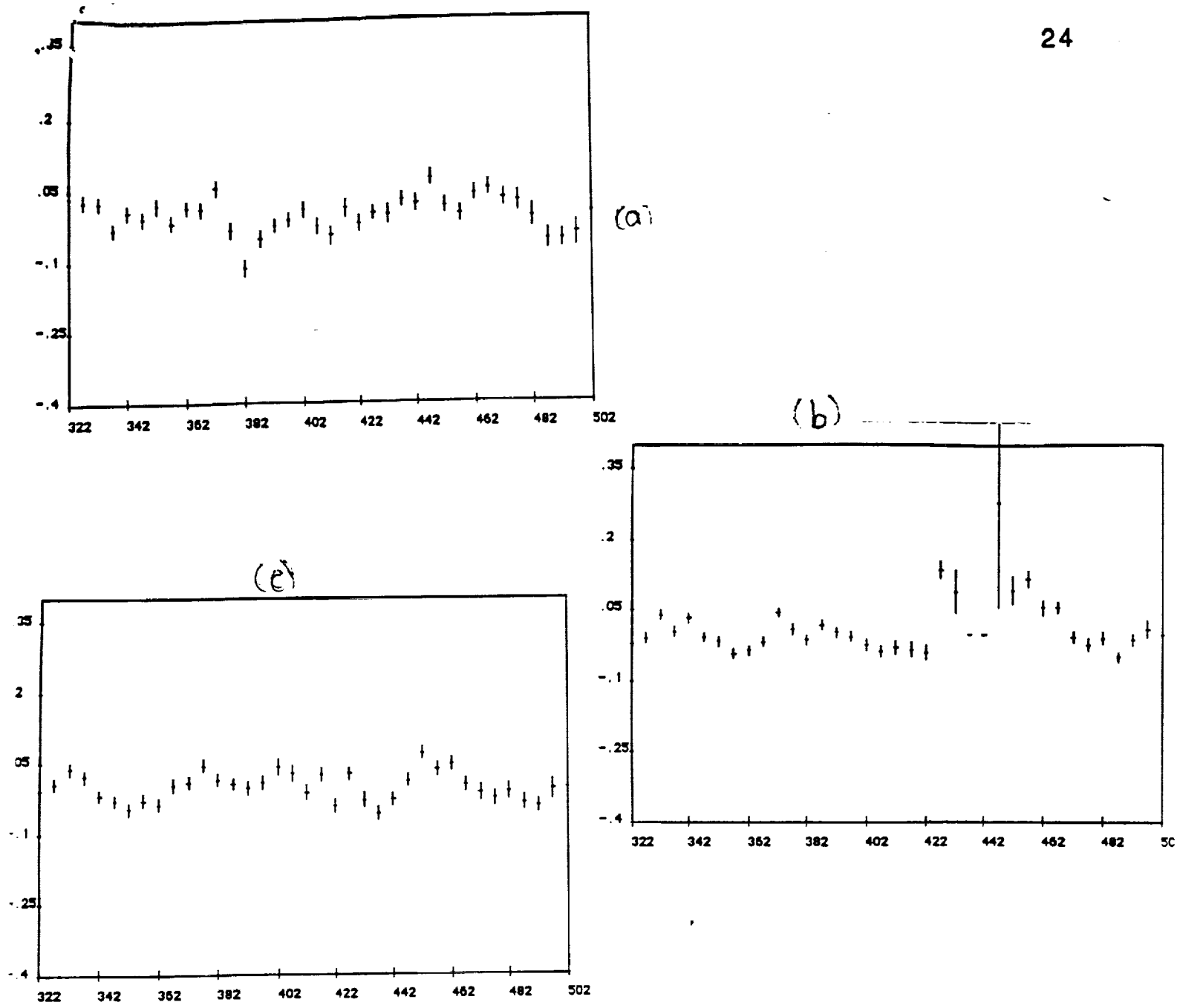

Figure 7. a) Data versus time from β=-90° - -30°. b) Data versus time from β=-30° - 30°. c) Data versus time from β=30° - 90°. The mean and time-drift is subtracted from the data. The plots are taken from the 3 x 1.5 degree map.